Electrically Insulated Catalyst-Ionomer Anode Interfaces towards Durable Alkaline Membrane Electrolyzers

Minkyoung Kwak,[1] Kasinath Ojha,[1] Meikun Shen,[1] and Shannon W. Boettcher[1,2*]

[1]*Oregon Center for Electrochemistry, Department of Chemistry and Biochemistry, University of Oregon, Eugene, OR, 97403, USA.*

[2]*Department of Chemical & Biomolecular Engineering and Department of Chemistry, University of California, Berkeley, and Energy Storage and Distributed Resources Division, Lawrence Berkeley National Laboratory, Berkeley, CA 94720, United States*

*Corresponding Author: boettcher@berkeley.edu

Abstract: Anion-exchange-membrane water electrolysis (AEMWE) is an emerging technology for scalable hydrogen production. AEMWE has poor durability when operating without supporting electrolyte due to the oxidation of ionomers and membranes in contact with anode oxygen evolution reaction (OER) catalyst. We report a new "passivated" anode architecture for AEMWE where OER catalysts and ionomers are physically separated with a thin film amorphous oxide coating that is electrically insulating but conductive to hydroxide ions. We find that 2–3 nm of HfO$_x$ passivation layers show sufficient hydroxide ion transport to minimally limit the cell performance while suppressing ionomer degradation with both Ir (500 mA·cm^{-2} for 40 h) and CoO$_x$ (1.0 A·cm^{-2} for 100 h) model porous-transport-layer-supported catalysts in AEMWE. This interfacial engineering approach guides electrode design to improve the durability of AEMWE, particularly for systems operating with pure water feed.

Table of Contents Graphic
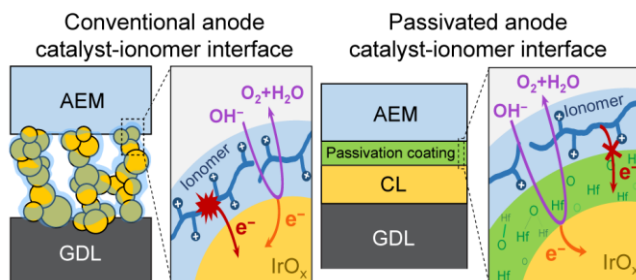
Article Text

Proton-exchange-membrane and alkaline water electrolysis (PEMWE and AWE) systems are the leading commercial technologies for green H_2 production. However, the locally acidic operating environment in PEMWE requires the use of expensive acid-stable catalysts, like IrO_2, and bipolar plates.[1-2] Fluorinated polymers are also used for the membrane/ionomer in PEMWE which might limit the deployment of PEM electrolyzers,[3] although this is likely manageable in the closed electrolyzer water loop. In contrast, AWE uses concentrated KOH electrolyte, with cheaper earth-abundant catalysts and flow fields / bipolar plates, thus lowering the system cost per electrode area. AWE, however, has traditional limitations in operating current density and hydrogen purity, crossover, and electrochemical pressurization.[4-5] Anion-exchange-membrane water electrolysis (AEMWE) is an emerging technology that, in principle, combines advantages for both PEMWE (zero-gap configuration with electrolyte-free water feed, no soluble electrolyte, differential pressure, variable load, etc.) and AWE systems (the use of inexpensive non-platinum-group-metal catalysts and cheap bipolar plates).[6-8]

While much effort has gone to anion-exchange membrane/ionomer development for AEMWE stability in the presence of the strong OH^- nucleophile,[9-13] as well as in catalyst development,[14-18] the durability of the system remains the primary limiting factor for commercialization and scale-up.[4, 8, 19-20] Supporting electrolyte KOH feed (typically 0.1 to 1 M KOH) has been used to compensate the substantial performance and durability loss from instable ionomer/membrane of pure-water AEMWE system,[21-22] and AEM electrolyzers with dilute KOH feed have been commercialized by Enapter.[23] The dilute KOH decreases the voltage degradation rate at least an order of magnitude compared to the pure water feed,[7, 21, 24] although the soluble electrolyte re-introduces some of the limitations of traditional AWE. For example, there are possible issues with increased balance-of-plant cost, shunt currents, and reverse polarizations on shutdown.[25-28]

In pure-water AEMWE, and likely also (to a lesser extent) in liquid-KOH AEMWE, the oxidative instability of ionomers/membranes at the anode driving the oxygen evolution reaction (OER) is a key durability issue.[29-31] The anode catalysts and ionomers are traditionally in direct contact in the catalyst layer, and thus ionomers must be stable under the simultaneously highly oxidizing and strongly alkaline environment. However, even fluorocarbon polymers like Nafion degrade under these conditions,[21] perhaps because the oxidative bias increases the rate of

nucleophilic attack by the hydroxide (Nafion ionomer is nominally stable at an acidic anode). These anode ionomer-degradation processes increase the overvoltage at the anode due to loss of active catalyst surface area and increased hydroxide-transport-related losses.

The oxidative instability of ionomers interfaced with catalysts might be mitigated by interfacial engineering strategies, for example, by adding a thin film of electrically insulating metal oxides between ionomer and catalysts that block the electron flow from ionomers to catalysts but permits ions to transport. Thin layers of SiO_x and other metal oxides have been coated on top of electrocatalysts to minimize the undesired catalyst degradation processes[32-37] (*i.e.*, dissolution, catalyst-particle coalescence, detachment, or chemical poisoning) with desirable permselectivity towards reactants to maintain the electrocatalytic activity.[38-39] Metal-oxide coatings on battery electrode materials have been similarly used to prevent chemical attack and improve lifetime and electrolyte stability under cycling.[40-41] Because reactive electrochemical interfaces are broadly important in technology, strategies for understanding and engineering interfacial layers to enhance durability are of significant value.

Here we investigate interfacial engineering to stabilize ionomer contacting the anode catalyst in AEMWE systems. We developed "passivated" anodes consisting of HfO_x-coated IrO_x or CoO_x nanostructured OER catalysts grown directly on the porous transport layer (PTL, sometimes also referred to as the gas diffusion layer or GDL). The model OER catalyst is prepared by thermal oxidation of an evaported metal layer on a stainless steel PTL. The interface is stabilized by adding HfO_x via atomic layer deposition (ALD), prior to fabricating and testing pure-water-fed AEMWE cells. The passivated anodes showed reduced interfacial anode-ionomer oxidation and improved durability with a small decrease in voltage efficiency compared to the unpassivated control devices. The electronic insulation of the passivation coatings was mapped with conductive-atomic force microscopy (c-AFM), and post-mortem XPS analysis showed that catalyst-ionomer interface was stabilized with the thin film of HfO_x. Other than inorganic-based materials, of which there are likely many with similar roles to HfO_x, PTFE additives have been incorporated in anode catalyst layers as oxidative-resistant binders, although ionic resistance from the non-ion-conducting PTFE led to poor performance.[21] We discuss strategies to improved passivation layers that are ideally electronically insulating, chemically stable, basic oxides that absorb protons from water providing free OH^- for conduction through the layer. These new concepts in catalyst-ionomer interfacial

engineering are likely to play a key role in AEMWE and other emerging electrochemical technologies where dynamic and reactive interfaces are central to performance.

Catalyst-Ionomer Interfaces. Figure 1 shows the AEMWE single-cell configuration with a conventional- and passivated-anode structure, along with their degradation and working mechanisms. Catalyst-coated electrodes and the AEMs are assembled and fed with pure water to generate H_2 and O_2 gas at the cathode and anode, respectively (Figure 1a). Conventional anodes are fabricated by spray-coating catalyst/ionomer ink onto porous PTLs prior to integrating with the membrane in the cell (Figure 1b). In a microscopic picture of the catalyst-ionomer interface, the ionomer conducts OH^-, facilitating the OER at the interface with the catalyst (Figure 1b.*i*). This direct physical contact, however, allows electrons to flow from ionomer to catalyst, leading to electrochemical oxidative degradation of ionomers (Figure 1b.*ii*).

We demonstrate a new type of passivated anode (Figure 1c) where a thin OER catalyst layer grown directly on a PTL is coated with a metal-oxide thin film, here HfO_x, prior to adding ionomer. This passivation layer is meant to allow the transport of hydroxide ions, due to the porosity in the amorphous oxide, but insulates (ideally) against direct electron transfer between catalysts and ionomers (Figure 1c.*i*). HfO_x was chosen as a passivation layer material because as an amorphous thin film it is electrically insulating (and thus used as a gate dielectric in the semiconductor industry),[42-43] it has high alkaline stability,[43] and probably suitable for ion transport as are other thin amorphous oxides[44] and oxide surfaces.[45-46] HfO_x can also be deposited using well-established procedures and precursors in robust, conformal films by atomic layer deposition (ALD);[47-48] a technique sufficiently cost-effective and scalable to be integrated into catalyst/PTL processes.[49-50]
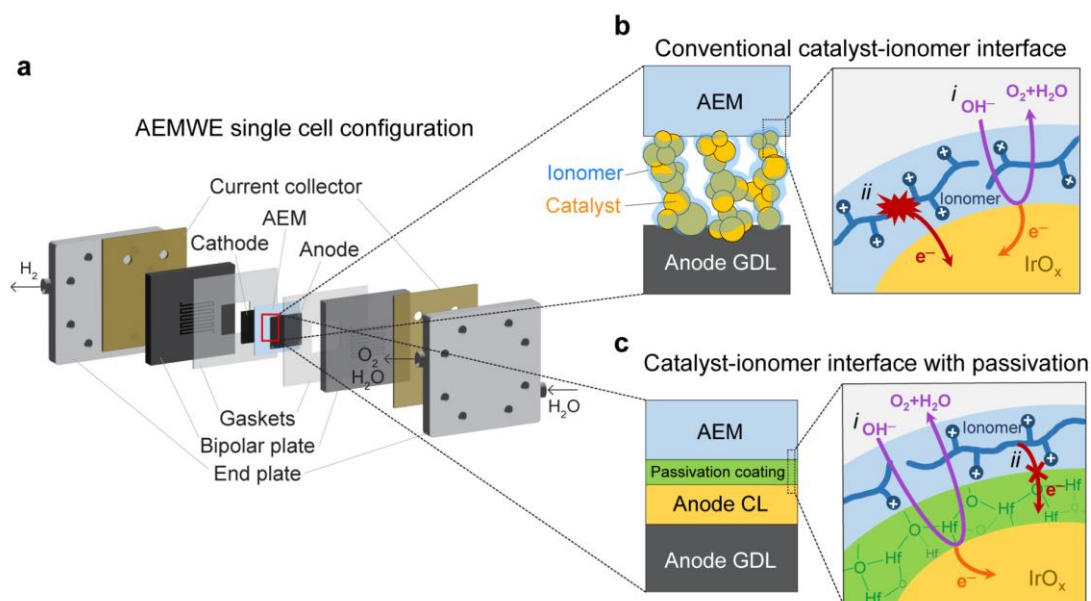
Figure 1. (a) AEMWE single-cell configuration. **(b)** Conventional anode structure interfacing bulk membrane with a corresponding microscopic picture of the catalyst-ionomer interface describing ionic and electronic processes: *i.* OH⁻ transport and OER, *ii.* oxidative ionomer degradation. **(c)** Passivated anode interfacing bulk membrane with a corresponding microscopic picture of the passivated catalyst-ionomer interface describing ionic and electronic processes: *i.* OH⁻ transport and OER with HfO_x coating and *ii.* suppression of ionomer degradation with an electronically insulating HfO_x layer.

Fabrication of model anodes. To study the effect of passivation coatings at the catalyst-ionomer interface, simplified Ir- and CoO_x-based anodes were built. In one case, A 75-nm layer of Ir metal was deposited on a stainless steel (SS) PTL as a catalyst layer using electron-beam evaporation. To enhance the performance of the Ir anode, we tried annealing the as-deposited samples to transform metallic Ir to iridium oxide. However, oxidation required ~600 °C to form iridium oxide (Figure S1) and concomitant oxidation of the SS PTL substrate apparently led to additional resistance. In another case, we deposited ~150 nm of Co on SS PTLs which were annealed at 300 °C to yield cobalt oxides which had better performance and stability (Figure S2). Scanning electron microscopy (SEM) images (Figures 2a and 2b) show uniform surface coverage and morphology of Ir and CoO_x catalyst layers on the SS GDLs. While the Ir catalyst layer was a continuous film with island-type particles on the SS GDL, the CoO_x catalyst layer developed nanostructured platelets on the SS PTL driven by thermal annealing and oxide crystallization. SEM cross-sectional images were obtained using focused ion beam (FIB) milling which illustrate the uniformity of the catalyst layers on SS GDLs. The thicknesses of Ir and CoO_x catalyst layers were

~75 nm and ~200 nm, respectively (Figures 2c and 2d). X-ray photoelectron spectroscopy (XPS) spectra of Ir 4f and Co 2p were used to assess the chemical state of the as-synthesized catalysts (Figures 2e and 2f).
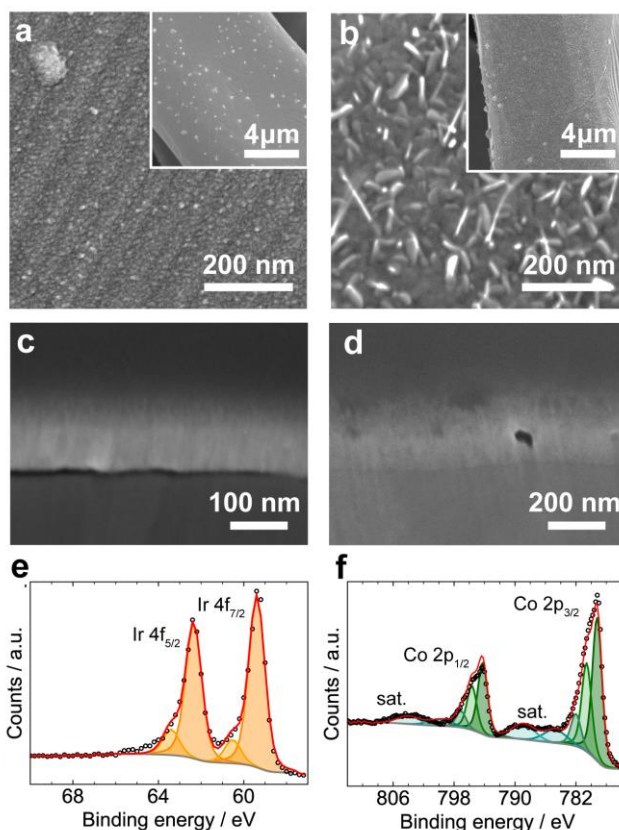
Figure 2. SEM images of **(a)** Ir-based electrode and **(b)** CoO_x-based electrode showing surface features. Cross-sectional SEM images of **(c)** Ir-based electrode and **(d)** CoO_x-based electrode. XP spectra of **(e)** Ir-based electrode and **(f)** CoO_x-based electrode. The XP spectra fits were made assuming metallic Ir with a surface oxide layer (Ir^{4+}) in Ir 4f spectra and mixed oxidation states of Co^{3+}/Co^{2+} in the Co 2p spectra (most likely forming Co_3O_4 after annealing).

Fabrication of passivation coatings. The anode passivation, a HfO_x thin film, was deposited on top of the catalyst layer using ALD. The thickness of the HfO_x controls the OH$^-$ transport and electron-insulating properties, as well as the electrochemical and mechanical stability of the films. Figure 3a shows a cross-sectional SEM image of a 2.5-nm-thick HfO_x-coated CoO_x electrode with a topcoat of PiperION ionomer. High-angle annular dark-field scanning transmission electron microscopy (HAADF-STEM) images with energy dispersive X-ray spectroscopy (EDS) mapping (Figure 3b) and a line-cut scan of elements (Figure 3c) show individual layers; a SS PTL, CoO_x catalyst, HfO_x passivation layer, and PiperION ionomer. The electrical insulation of HfO_x was tested using conducting atomic-force microscopy (c-AFM). Electrical current through the HfO_x on a partially coated Pt metal film was measured, along with height, under voltage bias. Figures 3d

and 3e show that ~2.5 nm of HfO$_x$ thin film was deposited on the Pt layer and that this nanoscale film is conformal enough to insulate the conductive Pt surface. Thickness-dependent c-AFM measurements are further shown in Figure S3.
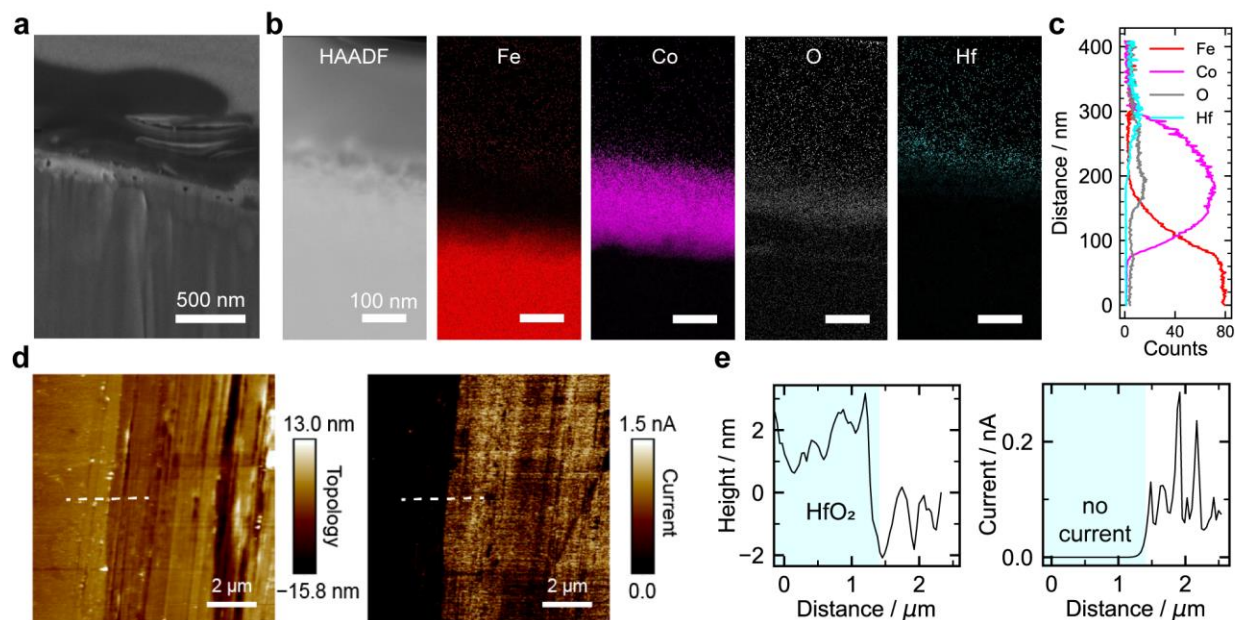
Figure 3. (a) Cross-sectional SEM image of CoO$_x$ anode with 2.5 nm of HfO$_x$ coating and a PiperION topcoat. **(b)** HAADF-STEM images of HfO$_x$ coated CoO$_x$ anode with EDS elemental maps of Fe, Co, O, and Hf (scale bars = 100 nm). **(c)** Line-cut STEM-EDS plot of Fe, Co, O, and Hf elements illustrating the layers. (d) AFM height (left) and current map (right) of 2.5 nm of HfO$_x$ on Pt/Ti on glass and (e) their corresponding line-cut plots.

Effect of passivation coating on Ir and Co system. PiperION, and other ionomers, are prone to oxidation when in contact with IrO$_x$ at oxygen evolution potentials.[30-31] We started with metallic Ir as a model catalyst to investigate the role of HfO$_x$ passivation layers on the oxidation process. Ir-based anodes, with HfO$_x$ coatings of 0.8, 3.5, 4.8, and 12 nm in thickness (calibrated based on thicknesses found on Si witness wafers placed in the same deposition process), were prepared and denoted as Ir-Hf0.8, Ir-Hf3.5, Ir-Hf4.8, and Ir-Hf12. The series of passivated anodes was evaluated in a 1 cm^2 AEMWE device. Before assembling the electrodes in the single cell, a thin layer of PiperION was spray-coated on the anode surface as a topcoat with a loading of 0.1–0.2 mg·cm^{-2} to improve ionic contact with the bulk PiperION membrane. All AEMWE tests were conducted in the electrolyzer hardware at 56 ± 1 °C with pure-water feed, while same cathode (Pt on carbon paper) and membrane (40-μm PiperION) materials were used to investigate the effects of passivation coatings on anodes in the cell. The temperature and materials were selected based on previous AEMWE literature with pure-water feed[21, 30-31] to establish a comparable model anode system to conventional nanoparticle-based anodes. The polarization curves obtained with uncoated

and HfO$_x$-coated Ir-based anodes are shown in Figure 4a. Compared to the unpassivated Ir-based anode, labeled as Ir, the HfO$_x$-passivated anodes initially performed worse. This is likely because of the additional ionic resistance across the HfO$_x$, leading to the cell voltage increasing by 0.8 V for the thickest 12 nm HfO$_x$ at 500 mA·cm^{-2}.

Electrochemical impedance spectroscopy (EIS) shows that the performance loss comes from an increase in apparent charge-transfer resistance with increasing HfO$_x$ thickness, rather than high frequency resistance (Figure 4b). This suggests the HfO$_x$ coatings led to decrease in the active surface area of Ir catalysts, blocking the active sites and affecting the OER activity of Ir electrodes, as opposed to contributing additional ohmic resistance. However, the durability data at 500 mA·cm^{-2} shows different cell-voltage degradation behavior of uncoated and HfO$_x$-coated Ir electrodes (Figure 4c). While the Ir control electrode, without any passivation layer, degraded rapidly (increasing voltage by ~0.3 V in 1 h), the HfO$_x$ passivated Ir anodes degraded slower even though they had higher initial cell voltages.

Cycle stability tests were also performed on fresh Ir anodes with and without HfO$_x$ passivation layers. The cell voltage was cycled between 0.6 V and 2.2 V, with a scan rate of 100 mV·s^{-1} to investigate the cell activation and degradation observed during the initial stages of the durability test (Figure S4a and S4d). Every 50 cycles, polarization and EIS data were obtained (Figure S4). The Ir sample without passivation showed significant performance loss, likely attributed to anode ionomer and catalyst/ionomer interface degradation. In contrast, the Ir-Hf3.5 sample showed performance improvement throughout the cycling test as well as reduction in charge-transfer resistance. This data is consistent with the need to control the reactive catalyst/ionomer interface for durability.

After 40 h of AEMWE operation at 500 mA·cm^{-2}, 3.5-nm-HfO$_x$-coated Ir had the lowest cell voltage of all Ir-devices tested. This result demonstrates the opportunity for durability improvement by implementing the passivation layers in the anode architecture. The Ir-Hf4.8 and Ir-Hf12 samples were operated at the lower current density of 200 mA·cm^{-2} and plotted in Figure S5a because of their high resistivity of HfO$_x$ coatings. Of the coatings tested here, 3.5 nm of ALD HfO$_x$ was thus found to be the best.

In a second series of devices, the CoO$_x$ on SS PTL annealed at 300 °C was compared to HfO$_x$-coated CoO$_x$ anodes similarly prepared and tested as previously but with a narrower range of HfO$_x$ thickness including 0.6, 1.1, 2.5, and 4.5 nm (CoO$_x$-Hf0.6, CoO$_x$ -Hf1.1, CoO$_x$ -Hf2.5, and CoO$_x$

-Hf4.5). To improve catalyst-membrane contact and achieve better cell performance, we used a dip-coating method, adopted from the literature,[51] to coat the nanoplatelet CoO_x-based electrodes with PiperION ionomer, which led to a higher loading of ionomer at ~1 mg·cm^{-2}. The effect of different ionomer topcoat preparation procedures is described in Figure S6.

The polarization curves of the bare CoO_x, and those coated with HfO_x, were tested in small 1 cm^2 AEMWE cells (Figure 4d). As with the Ir-based electrodes, the bare CoO_x electrode initially performed best, and the HfO_x caused incremental increases in initial cell voltage with thickness. Analysis of the impedance spectra shows that HfO_x increases the initial charge-transfer resistance (Figure 4e). During the durability test at 1 A·cm^{-2}, however, different cell voltage degradation rates (Figure 4f) were found. We decomposed the total cell voltage into anode and cathode contributions using a previously validated membrane-sensing reference electrode technique[52] (Figure S7 and Tables S1 and S2). While the anode voltage contributions were higher with the HfO_x-coated CoO_x electrodes than without the HfO_x coating, likely due to suppression of OER active sites requiring further interface engineering, the passivation layer did decrease the voltage degradation rate from 1.7 mV·h^{-1} for the uncoated sample to 0.7 mV·h^{-1} for CoO_x-Hf2.5.

Conventional nanoparticle-based anodes (Co_3O_4) were also prepared and operated at 1 A·cm^{-2} for comparison (Figure S8). The cell voltage degradation rate for the Co_3O_4 nanoparticle anode from the last 50 h was 2.3 mV·h^{-1}, higher than any of the uncoated or HfO_x-coated CoO_x-based electrodes, likely in part because the oxidative degradation is coupled to more-severe mechanical degradation for the powder catalyst-based electrodes.[21] Similar to the Ir-based electrode, AEMWE cycling tests on CoO_x anodes with and without the passivation layer were conducted (Figure S9). The CoO_x electrode without the HfO_x coating had the cell voltage increase from 2.22 V to 2.30 V at 1 A·cm^{-2} before and after 300 cycles, while CoO_x-Hf2.5 had the cell voltage decrease from 2.41 V to 2.28 V at 1 A·cm^{-2}. The passivation layer in this cycling experiment is likely stabilizing the interface and suppressing metal-oxide redox that may additionally contribute to interface morphological degradation on top of ionomer oxidation. The activation process with cycling is not fully understood.

Given the recent interest in KOH-fed AEMWE as a hybrid technology bridging conventional alkaline electrolysis with membrane technologies, selected anodes were tested in 0.1 M KOH at 75 °C (Figure S10) and 2 A·cm^{-2}. These conditions accelerate operative degradation modes. The passivated anodes showed higher initial operation voltages but lower degradation rates, consistent

with improved anode durability. We note that compared to tests in pure-water at lower current, additional degradation modes besides those at the anode may be operative that must be isolated and further addressed. We also note that we tested ALD TiO_x as an alternative passivation material candidate along with HfO_x, finding the HfO_x more promising in our screening test (Figure S11) in terms of ion-conducting (lower cell voltage) and electron insulating (less ionomer degradation) properties.
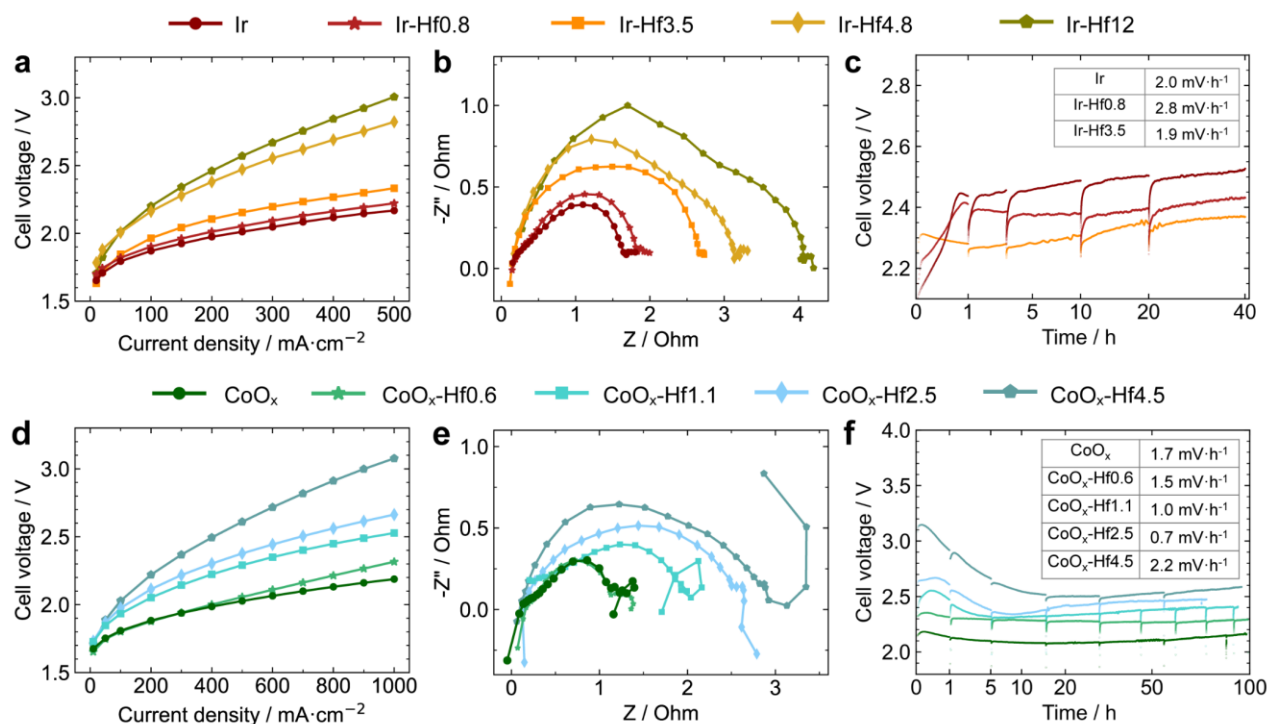
Figure 4. (a) Polarization curves of AEMWE cells with uncoated and HfO_x-coated Ir-based anodes, (b) corresponding EIS curves at a current density of 50 mA·cm^{-2} applied, and (c) durability test at a current density of 500 mA·cm^{-2} applied at 56 °C with pure water feed. Inset table summarizes cell voltage degradation rates from the last 20 h durability run. (d) Polarization curves of AEMWE cells with uncoated and HfO_x coated CoO_x-based anodes, (e) corresponding EIS curves at a current density of 50 mA·cm^{-2} applied, and (f) durability test at a current density of 1 A·cm^{-2} applied at 56 °C with pure water feed. Inset table summarizes cell voltage degradation rates from the last 50 h durability run. Ir samples were coated with ionomer using spray coating (~0.2 mg·cm^{-2} of loading). CoO_x-based samples were dip-coated with ionomer (loading ~1 mg·cm^{-2}). Only one of each type of different device was fabricated for this set of data.

Post-mortem analysis. XPS analysis was used to characterize the ionomer-related chemical species present before and after the durability tests at 500 mA·cm^{-2} for 40 h and at 1.0 A·cm^{-2} for 100 h for Ir and CoO_x samples, respectively. PiperION ionomer consists of a rigid aromatic carbon group. PiperION can be oxidized during AEMWE operation to lose charged nitrogen and fluorinated species and fragment the aromatic backbone (Figure 5a).[29, 53]

XP C-1s, F-1s and N-1s spectra of pristine PiperION on the Ir anode before AEMWE operation (Figure 5b) were decomposed into component chemical species including C–C/C=C and C–N for the C1s spectrum, quaternary ammonium for the N1s spectrum, and fluorinated carbon for the F1s spectrum. After 500 mA·cm^{-2} for 40 h, a more intense O–C=O peak at higher binding energy was observed and the main carbon peak broadened, suggesting oxidation and partial loss of ionomer backbone carbon. For N1s and F1s spectra, no obvious charged nitrogen and fluorinated species were found for the uncoated Ir sample. HfO$_x$ coatings on Ir samples (Ir-Hf0.8, Ir-Hf3.5) reduce the oxidation of carbon species after operation as evident from the C1s spectra. The charged nitrogen and fluorine peaks are also still observed for both Ir-Hf0.8 and Ir-Hf3.5. Those peaks remain more intense as the thickness of HfO$_x$ increases (Figure 5b). The sum of the XPS data shows that even under large oxidizing biases, the HfO$_x$ passivation layer substantially protects the ionomer. After operation, a new broad peak also appears in the C1s spectra for the Ir sample at binding energies above 296 eV from Ir 4d, which indicates the ionomer topcoat on bare Ir was mostly oxidized and flushed away. In contrast, the signal in this region is much weaker with the HfO$_x$, suggesting retention of the ionomer and a stabilized interface.

Comparing a bare CoO$_x$ electrode with a HfO$_x$-coated one after electrolyzer operation at 1.0 A·cm^{-2} for 100 h, the XP spectra show the suppression of ionomer degradation with HfO$_x$ (Figure 5c). A less-intense oxidized carbon peak is shown in the C1s spectra for both CoO$_x$-Hf1.1 and CoO$_x$-Hf2.5 compared to bare CoO$_x$. More-intense signals were obtained for charged nitrogen and fluorine peaks from the HfO$_x$-coated CoO$_x$ compared to the uncoated CoO$_x$, reflecting ionomer structures were better-retained with HfO$_x$ passivation. All these results are consistent with the passivation layer functioning to block the oxidative damage to the ionomer. Noticeably, a large broad new peak was observed in the nominal F1s spectra in samples after electrolyzer operation at binding energies higher than 696 eV, which is in the Auger region of Co. Co-Auger signal is suppressed when the HfO$_x$ coating is present indicating the ionomer and CoO$_x$ catalyst layers were physically separated. From the XP spectra collected before and after electrolyzer testing, the relative areal ratios of oxidized carbon peaks to total carbon peaks in the C 1s spectrum and charged nitrogen and fluorine peaks to total carbon peak in each sample are calculated and listed in Table S3. Ionomer oxidation is suppressed with HfO$_x$ coatings in both Ir and CoO$_x$ systems, respectively. In addition, even though there is no distinct trend observed in the ratio of N$^+$ or F

over total C peaks with the thickness of HfO$_x$, the calculated ratios of N$^+$ or F over total C are higher when the electrode surface is coated with HfO$_x$.

Ir-4f and Co-2p XP spectra were also collected and compared. During the cell operation, metallic Ir is oxidized as evident from the shift of the Ir peaks to higher binding energies after operation (Figure 6a). The degree of this change differs somewhat with HfO$_x$ coating thickness, yet all the films show oxidation of the Ir, consistent with the permeability of the thin HfO$_x$ to OH$^-$. The CoO$_x$ (Figure 6b), being already oxidized, are much less affected by cell operation having similar XP spectra for all samples. The Hf-4f spectra of Ir-Hf0.8, Ir-Hf3.5, CoO$_x$-Hf1.1, and CoO$_x$-Hf2.5, show the HfO$_x$ layers remain on the anodes even after the durability AEMWE cell test (Figure 6c). For comparison, the Hf 4f spectra of all samples before the cell operation are plotted in Figure S12.
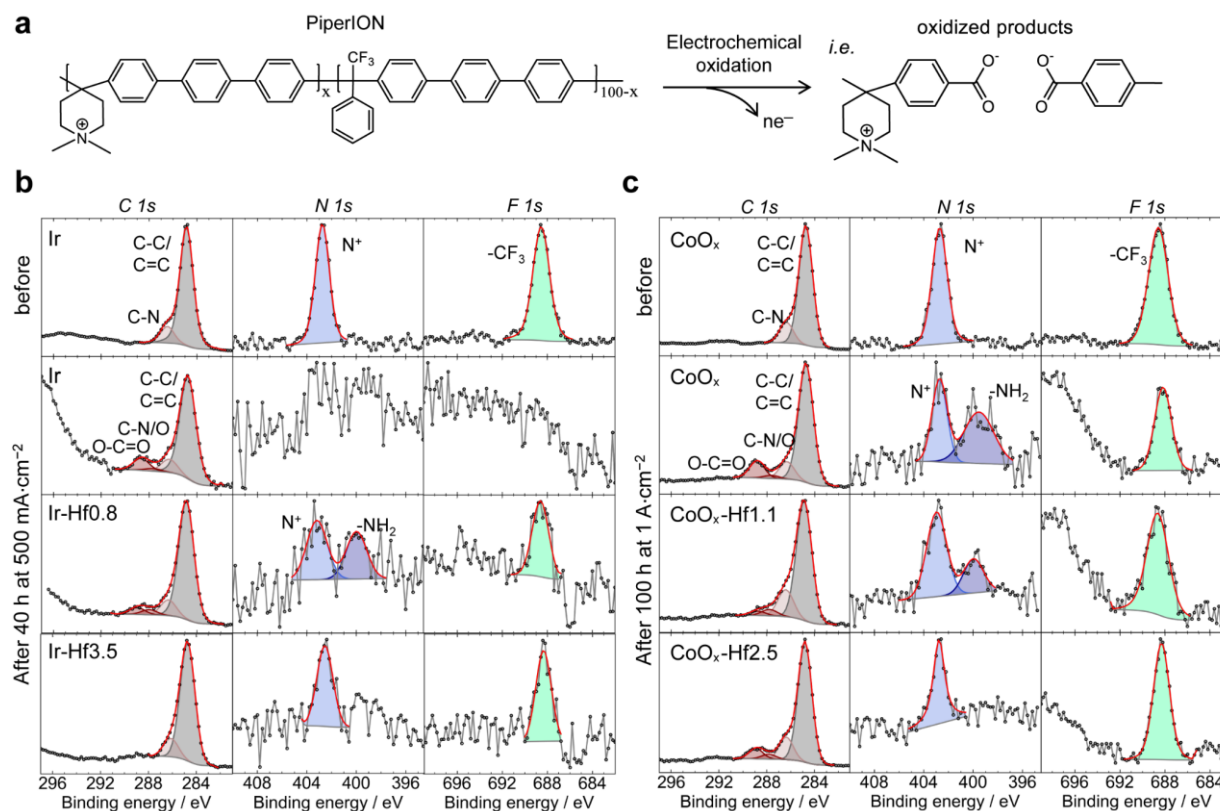
Figure 5. (a) PiperION structure and its exemplified electrochemical degradation products due to oxidation. **(b)** XP spectra of C 1s, N 1s, and F 1s of Ir the sample before and after cell operation and Ir-Hf0.8 and Ir-Hf3.5 samples after cell operation (500 mA·cm^{-2}, 40 h). **(c)** XP spectra of C 1s, N 1s, and F 1s of CoO$_x$ sample before and after cell operation and CoO$_x$-Hf1.1 and CoO$_x$ -Hf2.5 samples after cell operation (1.0 A·cm^{-2}, 100 h).

Because quantification is difficult with XPS, especially for the non-planar catalyst-coated PTLs studied here, we also used cross-sectional electron microscopy. The CoO_x-Hf2.5 anode after operating at 1.0 A·cm^{-2} for 100 h was characterized using FIB-SEM and HAADF-STEM/EDS (Figure 6d; compared to Figures 3a and 3b). In the cross-sectional view, ~200 nm of CoO_x is visible on the top of the SS surface, even after operation. High-resolution transmission-electron microscopy (HRTEM) analysis of the CoO_x layer shows lattice fringes probably corresponding Co_3O_4 (Figure S13).

From elemental mapping, we observe the SS PTL, CoO_x catalyst layer, and HfO_x passivation layer were largely preserved after 100 h of the electrolyzer testing at 1.0 A·cm^{-2}. The EDS spectra of CoO_x-Hf2.5 sample were taken before and after the electrolyzer operation showing the Hf signal remained after operating in the harsh oxidative environment (Figure S14). Importantly, the darker region (as marked in the SEM image of Figure 6d) is the ionomer layer which remains present after 100 h of electrolyzer test at 1.0 A·cm^{-2} (see EELS spectrum in Figure S15). Furthermore, for Ir-Hf12 sample, where HfO_x is thick enough to substantially impede hydroxide transport, after operating the anode at lower current density, we still observe the HfO_x layer using SEM-EDS (Figure S5b).
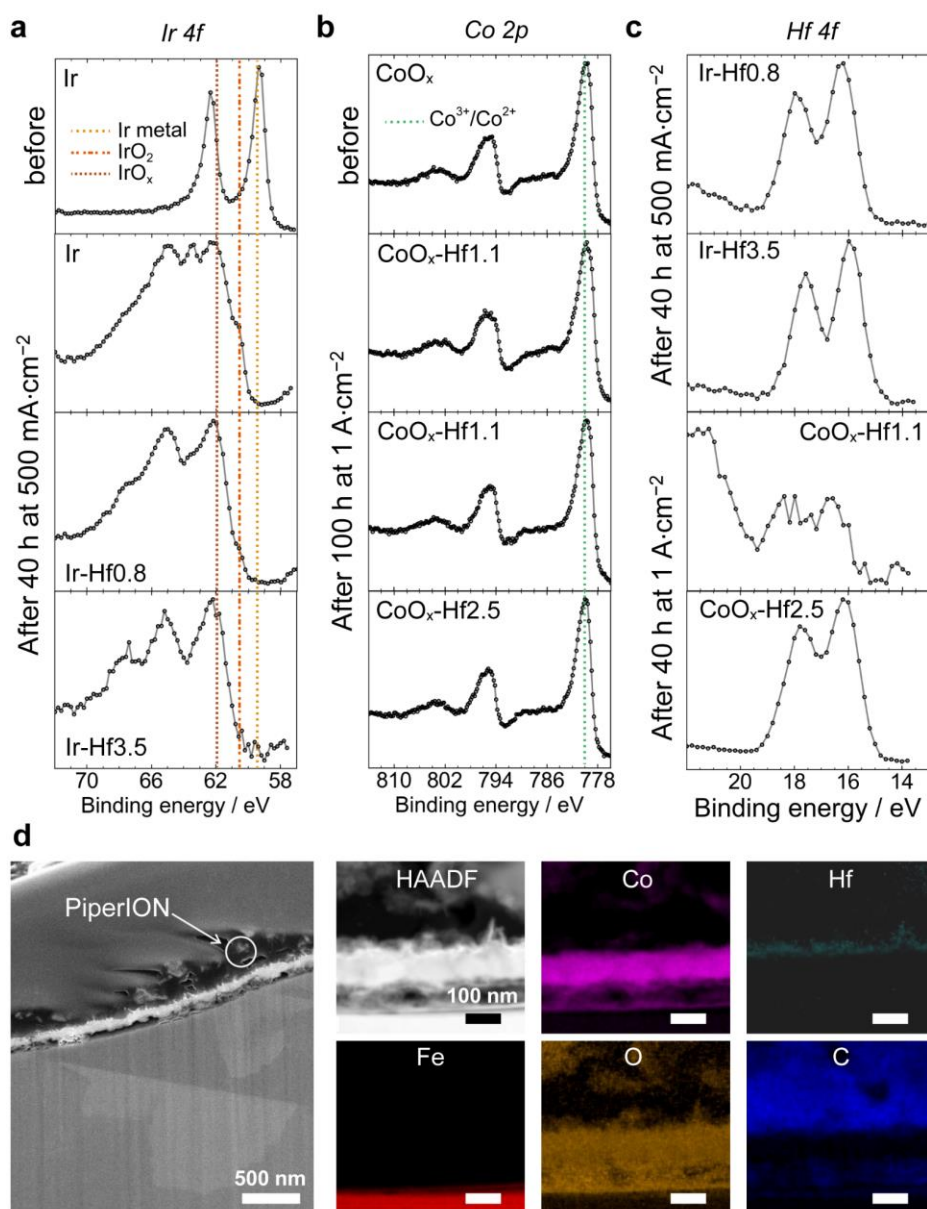
Figure 6. XPS spectra of **(a)** Ir-4f of Ir sample before and after cell operation and Ir-Hf0.8 and Ir-Hf3.5 samples after cell operation (500 mA·cm^{-2}, 40 h), **(b)** Co 2p spectra of CoO$_x$ sample before and after cell operation and CoO$_x$-Hf1.1 and CoO$_x$ -Hf2.5 samples after cell operation (1 A·cm^{-2}, 100 h), and **(c)** Hf 4f spectra of Ir-Hf0.8 and Ir-Hf3.5 samples after cell operation (500 mA·cm^{-2}, 40 h) and CoO$_x$-Hf1.1 and CoO$_x$-Hf2.5 samples after cell operation (1 A·cm^{-2}, 100 h). **(d)** Cross-sectional SEM image and HAADF-STEM images with EDS elemental maps of CoO$_x$-Hf2.5 sample operated at 1.0 A·cm^{-2} for 100 h (scale bars = 100 nm for elemental maps).

The behavior of HfO$_x$ coatings on the Ir- and CoO$_x$-based anodes can be explained by the various degradation mechanisms. There are often multiple reasons for voltage degradation, including: *i*) catalyst deactivation, dissolution, and detachment, *ii*) ionomer degradation and poisoning, *iii*) ion contamination, and *iv*) mechanical failure.[4, 19] The most-dominant factor for IrO$_x$

during the long-term test was ionomer oxidation, as reported previously.[31] Similarly, here we find ionomers are easily oxidized at the OER potential by Ir. When the Ir|ionomer interface is separated by HfO_x to form Ir|HfO_x|ionomer, less ionomer degradation occurs, and thus lower cell voltages and voltage degradation rates were observed. In contrast, CoO_x is a poor electrical conductor, and probably forms an interfacial oxyhydroxide spontaneously under operation. This appears to provide a more-stable interface with ionomer, and slower ionomer oxidation during operation. When we apply HfO_x on the CoO_x anode, the ionic and electrical resistances coming from HfO_x are relatively more important. Over longer time periods, slower degradation rates are still provided with the CoO_x|HfO_x|ionomer systems compared to CoO_x|ionomer. This result emphasizes the importance of interfacial engineering in AEMWE systems. However, we emphasize that conductive, metallic catalyst layers are obviously preferred in the porous electrode to reach the ultimate performance. However, as oxidation-resistant ionomers/membranes for AEMWE have not yet been developed, the ionomer-catalyst interface is prone to damage by oxidation from the catalyst. Conductive catalysts can both drive water oxidation and ionomer oxidation more efficiently over their entire surface area. Thus, we need to improve the catalyst-ionomer interface to fully exploit conductive and efficient anode catalysts.

In addition to ionomer degradation, catalyst degradation by dissolution can occur during electrolyzer operation. Ir-based OER catalysts are known to slowly leach during operation, and dissolution rates are faster for oxidized metallic Ir compared to crystalline rutile IrO_2.[54-56] It is possible that the added HfO_x layers may protect and stabilize the surface of the Ir catalyst layer from dissolution, leading to lower cell voltage in durability test data. The CoO_x model catalyst we prepared here appears stable in its oxide form and may have less dissolution under OER conditions intrinsically,[57] thus being less affected by the presence of the HfO_x coatings. While the scope of this study is the role of passivation coatings in ionomer degradation, further study focused on catalyst degradation/dissolution using on-line inductively coupled plasma mass spectrometry (ICP-MS)[58-59] would be helpful to determine the role of HfO_x, or other, coatings in stabilizing catalyst layer specifically.

In summary, a new passivated anode for AEMWE has been developed where the OER catalysts are directly deposited on the GDLs, and the surface of the catalysts is protected with thin films of ion-permeable but electron-blocking metal oxide films, here ALD HfO_x. The best working

thickness of HfO$_x$ coating found here was ~2–3 nm, where the HfO$_x$ layer is thin enough not to substantially limit the OH$^-$ transport through the layer, but thick enough to form a continuous film so that the ionomer degradation is suppressed, and the desirable mechanical stability of the film is maintained. The total-cell voltage degradation was suppressed with the presence of HfO$_x$ protective layers in the Ir-based system because of substantially lowered ionomer degradation and increased Ir layer stability at the anodes. For CoO$_x$-based anodes, although less ionomer degradation is confirmed with XPS analysis, the resistivity of HfO$_x$ increased the cell voltage for these model anodes. This work indicates that understanding and engineering the catalyst-ionomer interface is a promising and viable strategy to solve the limitations and problems in AEMWE development and additional work will apply these innovations to higher-surface-area catalysts designed for high-efficiency AEMWE. The concepts developed and employed here may also be useful for electrolyte-fed hybrid AWE/AEMWE systems.

Supporting Information: Experimental procedures and additional materials characterization and electrolyzer data

Author Information

Corresponding Author

Shannon W. Boettcher - *Department of Chemical & Biomolecular Engineering and Department of Chemistry, University of California, Berkeley, and Energy Storage and Distributed Resources Division, Lawrence Berkeley National Laboratory, Berkeley, CA 94720, United States; Oregon Center for Electrochemistry, University of Oregon, Eugene, OR, 97403, USA. boettcher@berkeley.edu*

Authors

Minkyoung Kwak - *Oregon Center for Electrochemistry, Department of Chemistry and Biochemistry, University of Oregon, Eugene, OR, 97403, USA.*

Kasinath Ojha – *Oregon Center for Electrochemistry, Department of Chemistry and Biochemistry, University of Oregon, Eugene, OR, 97403, USA.*

Meikun Shen - *Oregon Center for Electrochemistry, Department of Chemistry and Biochemistry, University of Oregon, Eugene, OR, 97403, USA.*

Author contributions

M.K., K.O. and S.W.B. designed the experiment and led the project. M.K. and K.O. prepared samples and collected electrolyzer data. M.K. conducted SEM and XPS measurement and analysis. K.O. led TEM data acquisition. M.S. performed conductive AFM characterization. M.K., K.O. and S.W.B. wrote the manuscript with input from all authors.

Acknowledgements

Reference

1. Ayers, K. E.; Anderson, E. B.; Capuano, C.; Carter, B.; Dalton, L.; Hanlon, G.; Manco, J.; Niedzwiecki, M., Research Advances towards Low Cost, High Efficiency PEM Electrolysis. *ECS Transactions* **2010,** *33* (1), 3-3.
2. Carmo, M.; Fritz, D. L.; Mergel, J.; Stolten, D., A Comprehensive Review on PEM Water Electrolysis. *Int. J. Hydrogen Energy* **2013,** *38* (12), 4901-4934.
3. Evich, M. G.; Davis, M. J. B.; McCord, J. P.; Acrey, B.; Awkerman, J. A.; Knappe, D. R. U.; Lindstrom, A. B.; Speth, T. F.; Tebes-Stevens, C.; Strynar, M. J.; Wang, Z.; Weber, E. J.; Henderson, W. M.; Washington, J. W., Per- and Polyfluoroalkyl Substances in the Environment. *Science* **2022,** *375* (6580), 9065-9065.
4. Li, D.; Motz, A. R.; Bae, C.; Fujimoto, C.; Yang, G.; Zhang, F. Y.; Ayers, K. E.; Kim, Y. S., Durability of Anion Exchange Membrane Water Electrolyzers. *Energy Environ. Sci.* **2021,** *14* (6), 3393-3419.
5. Ehlers, J. C.; Feidenhans'l, A. A.; Therkildsen, K. T.; Larrazábal, G. O., Affordable Green Hydrogen from Alkaline Water Electrolysis: Key Research Needs from an Industrial Perspective. *ACS Energy Lett.* **2023,** *8* (3), 1502-1509.
6. Vincent, I.; Bessarabov, D., Low cost hydrogen production by anion exchange membrane electrolysis: A review. *Renewable and Sustainable Energy Reviews* **2018,** *81*, 1690-1704.
7. Leng, Y.; Chen, G.; Mendoza, A. J.; Tighe, T. B.; Hickner, M. A.; Wang, C.-Y., Solid-state water electrolysis with an alkaline membrane. *J. Am. Chem. Soc.* **2012,** *134* (22), 9054-9057.
8. Henkensmeier, D.; Najibah, M.; Harms, C.; Žitka, J.; Hnát, J.; Bouzek, K., Overview: State-

of-the Art Commercial Membranes for Anion Exchange Membrane Water Electrolysis. *J. Electrochem. En. Conv. Stor* **2020,** *18* (2).

9. Mardle, P.; Chen, B.; Holdcroft, S., Opportunities of Ionomer Development for Anion-Exchange Membrane Water Electrolysis. *ACS Energy Lett.* **2023,** *8* (8), 3330-3342.

10. Li, D.; Park, E. J.; Zhu, W.; Shi, Q.; Zhou, Y.; Tian, H.; Lin, Y.; Serov, A.; Zulevi, B.; Baca, E. D.; Fujimoto, C.; Chung, H. T.; Kim, Y. S., Highly quaternized polystyrene ionomers for high performance anion exchange membrane water electrolysers. *Nat. Energy* **2020,** *5* (5), 378-385.

11. Kang, S. Y.; Park, J. E.; Jang, G. Y.; Kim, O.-H.; Kwon, O. J.; Cho, Y.-H.; Sung, Y.-E., High-Performance and Durable Water Electrolysis Using a Highly Conductive and Stable Anion-Exchange Membrane. *Int. J. Hydrogen Energy* **2022,** *47* (15), 9115-9126.

12. Chen, N.; Jiang, Q.; Song, F.; Hu, X., Robust Piperidinium-Enriched Polystyrene Ionomers for Anion Exchange Membrane Fuel Cells and Water Electrolyzers. *ACS Energy Lett.* **2023,** *8* (10), 4043-4051.

13. Song, W.; Peng, K.; Xu, W.; Liu, X.; Zhang, H.; Liang, X.; Ye, B.; Zhang, H.; Yang, Z.; Wu, L.; Ge, X.; Xu, T., Upscaled Production of an Ultramicroporous Anion-Exchange Membrane Enables Long-Term Operation in Electrochemical Energy Devices. *Nat. Commun.* **2023,** *14* (1), 2732.

14. Gong, M.; Li, Y.; Wang, H.; Liang, Y.; Wu, J. Z.; Zhou, J.; Wang, J.; Regier, T.; Wei, F.; Dai, H., An Advanced Ni–Fe Layered Double Hydroxide Electrocatalyst for Water Oxidation. *J. Am. Chem. Soc.* **2013,** *135* (23), 8452-8455.

15. Jeon, S. S.; Lim, J.; Kang, P. W.; Lee, J. W.; Kang, G.; Lee, H., Design Principles of NiFe-Layered Double Hydroxide Anode Catalysts for Anion Exchange Membrane Water Electrolyzers. *ACS Appl. Mater. Interfaces* **2021,** *13* (31), 37179-37186.

16. Choi, W.-S.; Jang, M. J.; Park, Y. S.; Lee, K. H.; Lee, J. Y.; Seo, M.-H.; Choi, S. M., Three-Dimensional Honeycomb-Like $Cu_{0.81}Co_{2.19}O_4$ Nanosheet Arrays Supported by Ni Foam and Their High Efficiency as Oxygen Evolution Electrodes. *ACS Appl. Mater. Interfaces* **2018,** *10* (45), 38663-38668.

17. Chen, D.; Park, Y. S.; Liu, F.; Fang, L.; Duan, C., Hybrid Perovskites as Oxygen Evolution Electrocatalysts for High-Performance Anion Exchange Membrane Water Electrolyzers. *Chemical Engineering Journal* **2023,** *452*, 139105-139105.

18. Zheng, Y.; Serban, A.; Zhang, H.; Chen, N.; Song, F.; Hu, X., Anion Exchange Ionomers Enable Sustained Pure-Water Electrolysis Using Platinum-Group-Metal-Free Electrocatalysts. *ACS Energy Lett.* **2023**, 5018-5024.

19. Xu, Q.; Zhang, L.; Zhang, J.; Wang, J.; Hu, Y.; Jiang, H.; Li, C., Anion Exchange Membrane Water Electrolyzer: Electrode Design, Lab-Scaled Testing System and Performance Evaluation. *EnergyChem* **2022,** *4* (5), 100087.

20. Lee, S. A.; Kim, J.; Kwon, K. C.; Park, S. H.; Jang, H. W., Anion Exchange Membrane Water Electrolysis for Sustainable Large-Scale Hydrogen Production. *Carbon Neutralization* **2022,** *1* (1), 26-48.

21. Lindquist, G. A.; Gaitor, J. C.; Thompson, W. L.; Brogden, V.; Noonan, K. J. T.; Boettcher, S. W., Oxidative instability of ionomers in hydroxide-exchange-membrane water electrolyzers. *Energy Environ. Sci.* **2023**, 4373-4387.

22. Andrew, W. T.; Jason, K. L.; Jason, R. S.; Nemanja, D.; Adam, Z. W.; Xiong, P., Design and Operating Principles for High-Performing Anion Exchange Membrane Water Electrolyzers. *J. Power Sources* **2023,** *567*, 232967.

23. Enapter, Enapter AG Unveils the World's First Megawatt-Class AEM Electrolyser.

24. Zhang, L.; Xu, Q.; Hu, Y.; Chen, L.; Jiang, H., Benchmarking the pH–Stability Relationship of Metal Oxide Anodes in Anion Exchange Membrane Water Electrolysis. *ACS Sutain.. Chem. Engin.* **2023,** *11* (36), 13251-13259.

25. Joseph Steven, L.; Sanggyu, K.; Hyun-Seok, C.; Chang-Hee, K.; Sirivatch, S., Impacts of Manifold Geometry and Flow Configuration on Shunt Current, Current Distributions, and Crossover in an Alkaline Electrolysis Stack. *ECS Meeting Abstracts* **2022,** *MA2022-01* (38), 1696.

26. Ashraf; Jinlei, H.; Kensaku, N.; Yoshiyuki, K.; Yoshinori, N.; Akihiro, K.; Takaaki, N.; Takuto, A.; Shigenori, M., Effects of operation and shutdown parameters and electrode materials on the reverse current phenomenon in alkaline water analyzers. *J. Power Sources* **2022,** *535*, 231454.

27. Uchino, Y.; Kobayashi, T.; Hasegawa, S.; Nagashima, I.; Sunada, Y.; Manabe, A.; Nishiki, Y.; Mitsushima, S., Relationship Between the Redox Reactions on a Bipolar Plate and Reverse Current After Alkaline Water Electrolysis. *Electrocatalysis* **2018,** *9* (1), 67-74.

28. Inc., I. I., Hydrogen Production Cost by AEM Water Electrolysis. In *FM-7024-A*.

29. Li, D.; Matanovic, I.; Lee, A. S.; Park, E. J.; Fujimoto, C.; Chung, H. T.; Kim, Y. S., Phenyl Oxidation Impacts the Durability of Alkaline Membrane Water Electrolyzer. *ACS Appl. Mater. Inter.* **2019,** *11* (10), 9696-9701.

30. Lindquist, G. A.; Oener, S. Z.; Krivina, R.; Motz, A. R.; Keane, A.; Capuano, C.; Ayers, K. E.; Boettcher, S. W., Performance and Durability of Pure-Water-Fed Anion Exchange Membrane Electrolyzers Using Baseline Materials and Operation. *ACS Appl. Mater. Interfaces* **2021,** *13* (44), 51917-51924.

31. Krivina, R. A.; Lindquist, G. A.; Beaudoin, S. R.; Stovall, T. N.; Thompson, W. L.; Twight, L. P.; Marsh, D.; Grzyb, J.; Fabrizio, K.; Hutchison, J. E.; Boettcher, S. W., Anode Catalysts in Anion-Exchange-Membrane Electrolysis without Supporting Electrolyte: Conductivity, Dynamics, and Ionomer Degradation. *Adv. Mater.* **2022,** *34* (35).

32. Bhardwaj, A. A.; Vos, J. G.; Beatty, M. E. S.; Baxter, A. F.; Koper, M. T. M.; Yip, N. Y.; Esposito, D. V., Ultrathin Silicon Oxide Overlayers Enable Selective Oxygen Evolution from Acidic and Unbuffered pH-Neutral Seawater. *ACS Catal.* **2021,** *11* (3), 1316-1330.

33. Esposito, D. V., Membrane-Coated Electrocatalysts—An Alternative Approach To Achieving Stable and Tunable Electrocatalysis. *ACS Catal.* **2018,** *8* (1), 457-465.

34. Maeda, K.; Teramura, K.; Lu, D.; Saito, N.; Inoue, Y.; Domen, K., Noble-Metal/Cr_2O_3 Core/Shell Nanoparticles as a Cocatalyst for Photocatalytic Overall Water Splitting. *Angew. Chem., Int. Ed.* **2006,** *45* (46), 7806-7809.

35. Finke, C. E.; Omelchenko, S. T.; Jasper, J. T.; Lichterman, M. F.; Read, C. G.; Lewis, N. S.; Hoffmann, M. R., Enhancing the activity of oxygen-evolution and chlorine-evolution electrocatalysts by atomic layer deposition of TiO_2. *Energy & Environmental Science* **2019,** *12* (1), 358-365.

36. Marichy, C.; Ercolano, G.; Caputo, G.; Willinger, M. G.; Jones, D.; Rozière, J.; Pinna, N.; Cavaliere, S., ALD SnO_2 Protective Decoration Enhances the Durability of a Pt Based Electrocatalyst. *J. Mater. Chem. A* **2016,** *4* (3), 969-975.

37. Tran-Phu, T.; Chen, H.; Daiyan, R.; Chatti, M.; Liu, B.; Amal, R.; Liu, Y.; Macfarlane, D. R.; Simonov, A. N.; Tricoli, A., Nanoscale TiO_2 Coatings Improve the Stability of an Earth-Abundant Cobalt Oxide Catalyst during Acidic Water Oxidation. *ACS Appl. Mater. Inter.* **2022**, 14, 29, 33130–33140

38. Vos, J. G.; Wezendonk, T. A.; Jeremiasse, A. W.; Koper, M. T. M., MnO$_x$/IrO$_x$ as Selective Oxygen Evolution Electrocatalyst in Acidic Chloride Solution. *J. Am. Chem. Soc.* **2018,** *140* (32), 10270-10281.

39. Obata, K.; Takanabe, K., A Permselective CeO$_x$ Coating To Improve the Stability of Oxygen Evolution Electrocatalysts. *Angew. Chem.* **2018,** *130* (6), 1632-1636.

40. Ramasamy, H. V.; Sinha, S.; Park, J.; Gong, M.; Aravindan, V.; Heo, J.; Lee, Y.-S., Enhancement of Electrochemical Activity of Ni-rich LiNi$_{0.8}$Mn$_{0.1}$Co$_{0.1}$O$_2$ by Precisely Controlled Al$_2$O$_3$ Nanocoatings via Atomic Layer Deposition. *J. Electrochem. Sci. Technol.* **2019,** *10* (2), 196-205.

41. Kazyak, E.; Chen, K.-H.; Chen, Y.; Cho, T. H.; Dasgupta, N. P., Enabling 4C Fast Charging of Lithium-Ion Batteries by Coating Graphite with a Solid-State Electrolyte. *Adv. Energy Mater.* **2022,** *12* (1), 2102618-2102618.

42. Kaufmann, I. R.; Pick, A.; Pereira, M. B.; Boudinov, H., Metal-insulator-SiC Schottky structures using HfO$_2$ and TiO$_2$ dielectrics. *Thin Solid Films* **2017,** *621*, 184-187.

43. Li, M.; Jin, Z. X.; Zhang, W.; Bai, Y. H.; Cao, Y. Q.; Li, W. M.; Wu, D.; Li, A. D., Comparison of Chemical Stability and Corrosion Resistance of Group IV Metal Oxide Films Formed by Thermal and Plasma-Enhanced Atomic Layer Deposition. *Scientific Reports* **2019,** *9* (1).

44. Chen, L.; Xu, Q.; Oener, S. Z.; Fabrizio, K.; Boettcher, S. W., Design Principles for Water Dissociation Catalysts in High-Performance Bipolar Membranes. *Nat. Commun.* **2022,** *13* (1), 3846.

45. Kosmulski, M., Attempt to Determine Pristine Points of Zero Charge of Nb$_2$O$_5$, Ta$_2$O$_5$, and HfO$_2$. *Langmuir* **1997,** *13*, 6315-6320.

46. Janusz, W., The Electrical Double Layer Parameters for the Group 4 Metal Oxide/Electrolyte System. *Adsorpt. Sci. Technol.* **2000,** *18*, 117-134.

47. Ritala, M.; Leskelä, M.; Niinistö, L.; Prohaska, T.; Friedbacher, G.; Grasserbauer, M., Development of Crystallinity and Morphology in Hafnium Dioxide Thin Films Grown by Atomic Layer Epitaxy. *Thin Solid Films* **1994,** *250* (1), 72-80.

48. Hausmann, D. M.; Kim, E. H.; Becker, J. S.; Gordon, R. G., Atomic Layer Deposition of Hafnium and Zirconium Oxides Using Metal Amide Precursors. *Chem. Mater.* **2002,** *14*, 4350-4358.

49. Chia-Hung, C.; Chien-Te, H.; Wen-Jie, K.; Li-Wei, L.; Yeou-Fu, L.; Hao-Wei, L.; Siyong, G.; Chun-Chieh, F.; Ruey-Shin, J.; Bikash Chandra, M.; Yasser Ashraf, G.; Cherng-Yuh, S., Roll-to-roll Atomic Layer Deposition of Titania Coating on Polymeric Separators for Lithium Ion Batteries. *J. Power Sources* **2021,** *482*, 228896.

50. Chang, N. L.; Poduval, G. K.; Sang, B.; Khoo, K.; Woodhouse, M.; Qi, F.; Dehghanimadvar, M.; Li, W. M.; Egan, R. J.; Hoex, B., Techno-Economic Analysis of the Use of Atomic Layer Deposited Transition Metal Oxides in Silicon Heterojunction Solar Cells. *Prog. Photovolt.: Res. Appl.* **2023,** *31* (4), 414-428.

51. Xiao, J.; Oliveira, A. M.; Wang, L.; Zhao, Y.; Wang, T.; Wang, J.; Setzler, B. P.; Yan, Y., Water-Fed Hydroxide Exchange Membrane Electrolyzer Enabled by a Fluoride-Incorporated Nickel-Iron Oxyhydroxide Oxygen Evolution Electrode. *ACS Catal.* **2021,** *11* (1), 264-270.

52. Xu, Q.; Oener, S. Z.; Lindquist, G.; Jiang, H.; Li, C.; Boettcher, S. W., Integrated Reference Electrodes in Anion-Exchange-Membrane Electrolyzers: Impact of Stainless-Steel Gas-Diffusion Layers and Internal Mechanical Pressure. *ACS Energy Lett.* **2021,** *6* (2), 305-312.

53. Krivina, R. A.; Lindquist, G. A.; Yang, M. C.; Cook, A. K.; Hendon, C. H.; Motz, A. R.; Capuano, C.; Ayers, K. E.; Hutchison, J. E.; Boettcher, S. W., Three-Electrode Study of Electrochemical Ionomer Degradation Relevant to Anion-Exchange-Membrane Water Electrolyzers. *ACS Appl. Mater. Inter.* **2022,** *14* (16), 18261-18274.

54. Kasian, O.; Grote, J.-P.; Geiger, S.; Cherevko, S.; Mayrhofer, K. J. J., The Common Intermediates of Oxygen Evolution and Dissolution Reactions during Water Electrolysis on Iridium. *Angew. Chem.* **2018,** *130* (9), 2514-2517.

55. Lončar, A.; Escalera-López, D.; Cherevko, S.; Hodnik, N., Inter-Relationships between Oxygen Evolution and Iridium Dissolution Mechanisms. *Angew. Chem. Int. Ed.* **2022,** *61*.

56. Geiger, S.; Kasian, O.; Ledendecker, M.; Pizzutilo, E.; Mingers, A. M.; Fu, W. T.; Diaz-Morales, O.; Li, Z.; Oellers, T.; Fruchter, L.; Ludwig, A.; Mayrhofer, K. J. J.; Koper, M. T. M.; Cherevko, S., The stability number as a metric for electrocatalyst stability benchmarking. *Nat. Catal.* **2018,** *1* (7), 508-515.

57. Kreider, M. E.; Burke Stevens, M., Material Changes in Electrocatalysis: An In Situ/Operando Focus on the Dynamics of Cobalt-Based Oxygen Reduction and Evolution Catalysts. *ChemElectroChem* **2023,** *10* (3), e202200958.

58. Krivina, R. A.; Zlatar, M.; Stovall, T. N.; Lindquist, G. A.; Escalera-López, D.; Cook, A. K.; Hutchison, J. E.; Cherevko, S.; Boettcher, S. W., Oxygen Evolution Electrocatalysis in Acids: Atomic Tuning of the Stability Number for Submonolayer IrOx on Conductive Oxides from Molecular Precursors. *ACS Catal.* **2023,** *13* (2), 902-915.

59. Schalenbach, M.; Kasian, O.; Ledendecker, M.; Speck, F. D.; Mingers, A. M.; Mayrhofer, K. J. J.; Cherevko, S., The Electrochemical Dissolution of Noble Metals in Alkaline Media. *Electrocatalysis* **2018,** *9* (2), 153-161.